

Neural Re-rendering for Full-frame Video Stabilization

YU-LUN LIU, National Taiwan University, MediaTek Inc.

WEI-SHENG LAI, Google

MING-HSUAN YANG, Google, UC Merced

YUNG-YU CHUANG, National Taiwan University

JIA-BIN HUANG, Virginia Tech

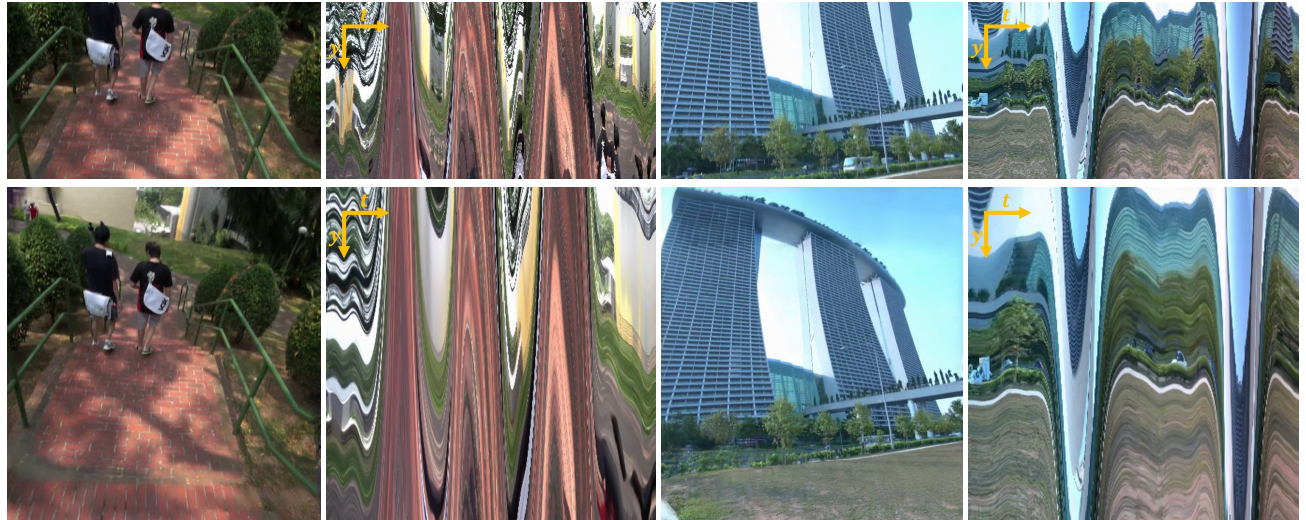


Fig. 1. **Full-frame video stabilization of challenging videos.** Our method takes a shaky input video (*top*) and produces a stabilized and distortion-free video (*bottom*), as indicated by less fluctuation in the $y-t$ epipolar plane image. Furthermore, by robustly fusing multiple neighboring frames, our results do not suffer from aggressive cropping of frame borders in the stabilized video and can even expand the field of view of the original video. Our approach significantly outperforms representative state-of-the-art video stabilization algorithms on these challenging scenarios (see Fig. 2).

Existing video stabilization methods either require aggressive cropping of frame boundaries or generate distortion artifacts on the stabilized frames. In this work, we present an algorithm for full-frame video stabilization by first estimating dense warp fields. Full-frame stabilized frames can then be synthesized by fusing warped contents from neighboring frames. The core technical novelty lies in our learning-based hybrid-space fusion that alleviates artifacts caused by optical flow inaccuracy and fast-moving objects. We validate the effectiveness of our method on the NUS and selfie video datasets. Extensive experiment results demonstrate the merits of our approach over prior video stabilization methods.

CCS Concepts: • Computing methodologies → Image processing; • Computer systems organization → Neural networks.

Additional Key Words and Phrases: video stabilization, neural rendering, deep learning

Permission to make digital or hard copies of all or part of this work for personal or classroom use is granted without fee provided that copies are not made or distributed for profit or commercial advantage and that copies bear this notice and the full citation on the first page. Copyrights for components of this work owned by others than ACM must be honored. Abstracting with credit is permitted. To copy otherwise, or republish, to post on servers or to redistribute to lists, requires prior specific permission and/or a fee. Request permissions from permissions@acm.org.

© 2024 Association for Computing Machinery.

XXXX-XXXX/2024/12-ART \$15.00

<https://doi.org/10.1145/nnnnnnnnnnnnnn>

ACM Reference Format:

Yu-Lun Liu, Wei-Sheng Lai, Ming-Hsuan Yang, Yung-Yu Chuang, and Jia-Bin Huang. 2024. Neural Re-rendering for Full-frame Video Stabilization. 1, 1 (December 2024), 12 pages. <https://doi.org/10.1145/nnnnnnnnnnnnnn>

1 INTRODUCTION

Video stabilization has become increasingly important with the rapid growth of video content on the Internet platforms, such as YouTube, Vimeo, and Instagram. Casually captured cellphone videos without a professional video stabilizer are often shaky and unpleasant to watch. These videos pose significant challenges for video stabilization algorithms. For example, videos are often noisy due to small image sensors, particularly in low-light environments. Handheld captured videos may contain large camera shake/jitter, resulting in severe motion blur and wobble artifacts from a rolling shutter camera.

Existing video stabilization methods usually consist of three main components: 1) motion estimation, 2) motion smoothing and 3) stable frame generation. First, the motion estimation step involves estimating motion through 2D feature detection/tracking [Goldstein and Fattal 2012; Lee et al. 2009; Liu et al. 2011; Wang et al. 2013], dense flow [Yu and Ramamoorthi 2019, 2020], or recovering camera motion and scene structures [Buehler et al. 2001a; Liu et al.

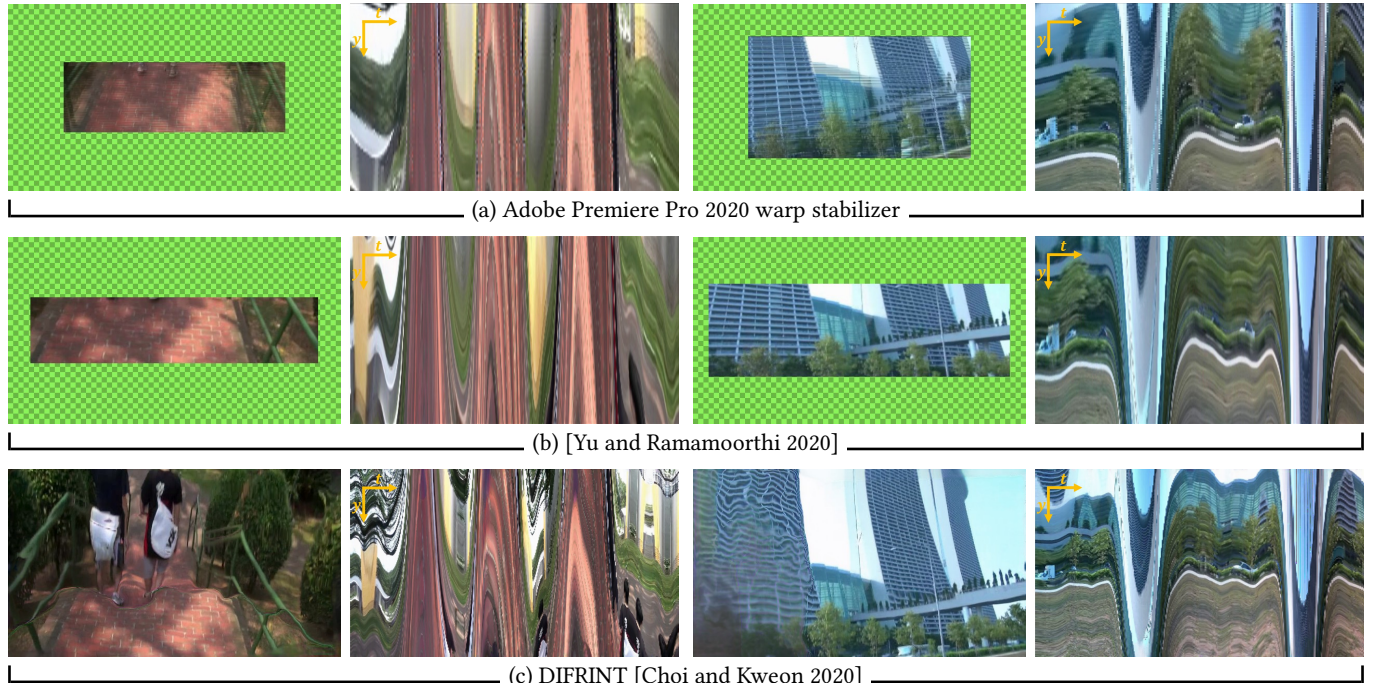


Fig. 2. Limitations of current state-of-the-art video stabilization techniques. (a) Current commercial video stabilization software (Adobe Premiere Pro 2020) fails to generate smooth video in challenging scenarios of rapid camera shakes. (b) The method in [Yu and Ramamoorthi 2020] produces temporally smooth video. However, the warped (stabilized) video contains many missing pixels at frame borders and inevitably requires applying aggressive cropping (green checkerboard areas) to generate a rectangle video. (c) The DIFRINT method [Choi and Kweon 2020] achieves full-frame video stabilization by iteratively applying frame interpolation to generate in-between, stabilized frames. However, interpolating between frames with large camera motion and moving occlusion is challenging. Their results are thus prone to severe artifacts.

2009, 2012; Smith et al. 2009; Zhou et al. 2013]. Second, the motion smoothing step then removes the high-frequency jittering in the estimated motion and predicts the spatial transformations to stabilize each frame in the form of homography [Matsushita et al. 2005], mixture of homography [Grundmann et al. 2012; Liu et al. 2013], or per-pixel warp fields [Liu et al. 2014; Yu and Ramamoorthi 2019, 2020]. Third, the stable frame generation step uses the predicted spatial transform to synthesize the stabilized video. The stabilized frames, however, often contain large missing regions at frame borders, particularly when videos with large camera motion. This forces existing methods to apply aggressive cropping for maintaining a rectangular frame and therefore leads to a significantly zoomed-in video with resolution loss (Fig. 2(a) and (b)).

Full-frame video stabilization methods aim to address the above-discussed limitation and produce stabilized video with the same field of view (FoV). One approach for full-frame video stabilization is to first compute the stabilized video (with missing pixels at the frame borders) and then apply flow-based video completion methods [Gao et al. 2020; Huang et al. 2016; Matsushita et al. 2005] to fill in missing contents. Such two-stage methods may suffer from the inaccuracies in flow estimation and inpainting (e.g., in poorly textured regions, fluid motion, and motion blur). A recent learning-based method, DIFRINT [Choi and Kweon 2020], instead uses iterative frame interpolation to stabilize the video while maintaining the original FoV.

However, we find that applying frame interpolation repeatedly leads to severe distortion and blur artifacts in challenging cases (Fig. 2(c)).

In this paper, we present a new algorithm that takes a shaky video and the estimated smooth motion fields for stabilization as inputs and produces a full-frame stable video. The core idea of our method lies in fusing information from multiple neighboring frames in a robust manner. Instead of using color frames directly, we use a learned CNN representation to encode rich local appearance for each frame, fuse multiple aligned feature maps, and use a neural decoder network to render the final color frame. We explore multiple design choices for fusing and blending multiple aligned frames (commonly used in image stitching and view synthesis applications). We then propose a hybrid fusion mechanism that leverages both feature-level and image-level fusion to alleviate the sensitivity to flow inaccuracy. In addition, we improve the visual quality of synthesized results by learning to predict spatially varying blending weights, removing blurry input frames for sharp video generation, and transferring high-frequency details residual to the re-rendered, stabilized frames. Our method generates stabilized video with significantly fewer artifacts and distortions while retaining (or even expanding) the original FoV (Fig. 1). We evaluate the proposed algorithm with the state-of-the-art methods and commercial video stabilization software (Adobe Premiere Pro 2020 warp stabilizer). Extensive experiments show that our method performs favorably

against existing methods on two public benchmark datasets [Liu et al. 2013; Yu and Ramamoorthi 2018].

The main contributions of this work are:

- We apply neural rendering techniques in the context of video stabilization to alleviate the issues of sensitivity to flow inaccuracy.
- We present a hybrid fusion mechanism for combining information from multiple frames at both feature- and image-level. We systematically validate various design choices through ablation studies.
- We demonstrate favorable performance against representative video stabilization techniques on two public datasets. We will release the source code to facilitate future research.

2 RELATED WORK

Motion estimation and smoothing. Most video stabilization methods focus on estimating motion between frames and smoothing the motion. For motion estimation, existing methods often estimate the motion in the 2D image space using sparse feature detection/tracking and dense optical flow. These methods differ in motion modeling, e.g., eigen-trajectories [Liu et al. 2011], epipolar geometry [Goldstein and Fattal 2012], warping grids [Liu et al. 2013], or dense flow fields [Yu and Ramamoorthi 2020]. For motion smoothing, prior methods use low-pass filtering [Liu et al. 2011], L1 optimization [Grundmann et al. 2011], and spatio-temporal optimization [Wang et al. 2013].

In contrast to estimating 2D motion, several methods recover the camera motion and proxy scene geometry by leveraging Structure from Motion (SfM) algorithms. These methods stabilize frames using 3D reconstruction and projection along with image-based rendering [Kopf et al. 2014] or content-preserving warps [Buehler et al. 2001a; Goldstein and Fattal 2012; Liu et al. 2009]. However, SfM algorithms are less effective in handling complex videos with severe motion blur and highly dynamic scenes. Specialized hardware such as depth cameras [Liu et al. 2012] or light field cameras [Smith et al. 2009] may be required for reliable pose estimation.

Deep learning-based approaches have recently been proposed to directly predict warping fields [Wang et al. 2018; Xu et al. 2018] or optical flows [Yu and Ramamoorthi 2019, 2020] for video stabilization. In particular, methods with dense warp fields [Liu et al. 2014; Yu and Ramamoorthi 2019, 2020] offer greater flexibility for compensating motion jittering and implicitly handling rolling shutter effects than parametric warp fields [Wang et al. 2018; Xu et al. 2018].

Our work builds upon existing 2D motion estimation/techniques for stabilization and focuses on synthesizing *full-frame* video outputs. Specifically, we adopt the state-of-the-art flow-based stabilization method [Yu and Ramamoorthi 2020] and use the estimated per-frame warped fields as inputs to our method¹.

Image fusion and composition. With the estimated and smoothed motion, the final step of video stabilization is to render the stabilized frames. Most existing methods synthesize frames by directly warping each input frame to the stabilized location using smoothed warping grids [Liu et al. 2011, 2013] or flow fields predicted by

¹Our method is agnostic to the motion smoothing techniques. Other approaches such as parametric warps can also be applied.

CNNs [Yu and Ramamoorthi 2019, 2020]. However, such approaches inevitably synthesize images with missing regions around frame boundaries. To maintain a rectangle shape, existing methods often crop off the blank areas and generate output videos with a lower resolution than the input video. To address this issue, full-frame video stabilization methods aim to stabilize videos without cropping. These methods use neighboring frames to fill in the blank and produce full-frame results by 2D motion inpainting [Gao et al. 2020; Gleicher and Liu 2008; Matsushita et al. 2005]. In contrast to existing motion inpainting methods that first generate stabilized frames then filling in missing pixels, our method leverage neural rendering to encode and fuse warped appearance features and learn to decode the fused feature map to the final color frames.

Several recent methods can generate full-frame stabilized videos without explicit motion estimation. For example, the method in [Wang et al. 2018] train a CNN with collected unstable-stable pairs to directly synthesize stable frames. However, direct synthesis of output frames without spatial transformations remains challenging. Recently, the DIFRINT method [Choi and Kweon 2020] generates full-frame stable videos by iteratively applying frame interpolation. This method couples motion smoothing and frame rendering together. However, the repeated frame interpolation often introduces visible distortion and artifacts (see Fig. 2(c)).

View synthesis. View synthesis algorithms aims to render photo-realistic images from novel viewpoints a single image [Kopf et al. 2020; Niklaus et al. 2019; Shih et al. 2020; Wiles et al. 2020; Wu et al. 2020] or multiple posed images [Chaurasia et al. 2013; Gortler et al. 1996; Hedman et al. 2018; Levoy and Hanrahan 1996; Penner and Zhang 2017; Riegler and Koltun 2020a,b]. These methods mainly differ in the ways to map and fuse information, e.g., view interpolation [Chen and Williams 1993; Debevec et al. 1996; Seitz and Dyer 1996], 3D proxy geometry and mapping [Buehler et al. 2001b], 3D multi-plane image [Srinivasan et al. 2019; Zhou et al. 2018], and CNN [Hedman et al. 2018; Riegler and Koltun 2020a,b]. Our fusion network resembles the encoder-decoder network used in [Riegler and Koltun 2020a] for view synthesis. However, our method does not require estimating scene geometry, which is challenging for dynamic scenes in video stabilization.

A recent line of research focuses on rendering novel views for *dynamic* scenes from a single video [Li et al. 2020; Tretschk et al. 2020; Xian et al. 2020] based on neural volume rendering [Lombardi et al. 2019; Mildenhall et al. 2020]. These methods can be used for full-frame video stabilization by rendering the dynamic video from a smooth camera trajectory. While promising results have been shown, these methods require per-video training and precise camera pose estimates. In contrast, our video stabilization method applies to a wider variety of videos.

Neural rendering. A direct blending of multiple images in the image space may lead to glitching artifacts (visible seams). Some recent methods train neural scene representations to synthesize novel views, such as NeRF [Mildenhall et al. 2020], scene representation networks [Sitzmann et al. 2019b], neural voxel grid [Lombardi et al. 2019; Sitzmann et al. 2019a], 3D Neural Point-Based Graphics [Aliev et al. 2020], and neural textures [Thies et al. 2019]. However, these methods often require time-consuming per-scene training and do

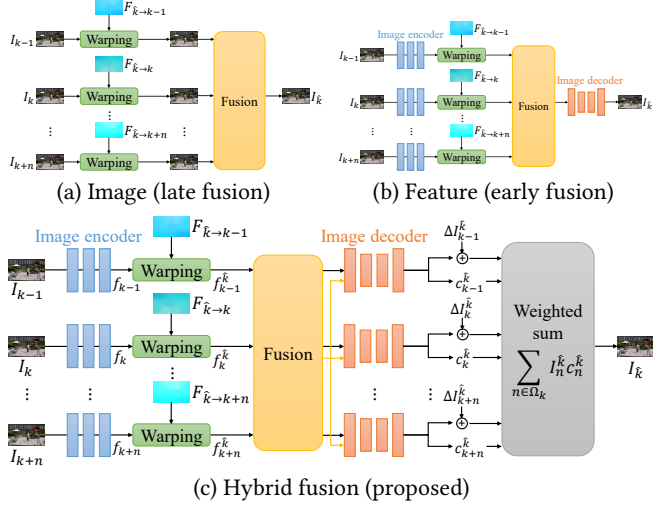


Fig. 3. Design choices for fusing multiple frames. To synthesize full-frame stabilized video, we need to *align* and *fuse* the contents from multiple neighboring frames in the input shaky video. (a) Conventional panorama image stitching (or in general image-based rendering) methods often fuse the warped (stabilized) images in the *image level*. Fusing in image-level works well when the alignment is accurate, but may generate blending artifacts (e.g., visible seams) when flow estimates are not reliable. (b) One can also encode the images as abstract CNN features, perform the fusion in the feature-space, and learn a decoder to convert the fused feature to output frames. Such approaches are more robust to flow inaccuracy but often produce overly blurred images. (c) Our proposed combines the advantages of both strategies. We first extract abstract image features (Eq. (6)). We then fuse the warped features from multiple frames. For each source frame, we take the fused feature map together with the individual warped features and decode it to the output frames and the associated confidence maps. Finally, we produce the final output frame by using the weighted average of the generated images as in Eq. (8).

not handle dynamic scenes. Our method does not require per-video finetuning.

3 FULL-FRAME VIDEO STABILIZATION

We denote I_t the frame in the real (unstabilized) camera space and I_t^k the frame in the virtual (stabilized) camera space at a timestamp t . Given an input video with T frames $\{I_t\}_{t=1}^T$, our goal is to generate a video $\{I_t^k\}_{t=1}^T$ that is visually stable and maintains the same FOV as the input video without any cropping. Existing video stabilization methods often apply a certain amount of cropping to exclude any missing pixels due to frame warping, as shown in Fig. 2. In contrast, we utilize the information from neighboring frames to render stabilized frames with completed contents or even expanding the FOV of the input video.

Video stabilization methods typically consist of three stages: 1) motion estimation, 2) motion smoothing, and 3) frame warping/rendering. Our method focuses on the third stage for rendering high-quality frames without any cropping. Our proposed algorithm is thus agnostic to particular motion estimation/smooth techniques. We assume that the warping field from the real camera space to the

virtual camera space is available for each frame (e.g., from [Yu and Ramamoorthi 2020]).

Given an input video, we first encode image features for each frame, warp the neighboring frames to the virtual camera space at the specific target timestamp, and then fuse the features to render a stabilized frame. We describe the technical detail of each step in the following sections.

3.1 Pre-processing

Motion estimation and smoothing. Several motion estimation and smoothing methods have been developed [Liu et al. 2011, 2013; Yu and Ramamoorthi 2020]. In this work, we use the state-of-the-art method [Yu and Ramamoorthi 2020] to obtain a backward dense warping field $F_{k \rightarrow \hat{k}}$ for each frame, where k indicates the input and \hat{k} denotes the stabilized output. Note that one can also generate the warping fields from other parametric motion models such as homography or affine. These warping fields can be directly used to warp the input video. However, the stabilized video often contains irregular boundaries and large portion of missing pixels. Therefore, the output video requires aggressive cropping and thus lose some contents.

Optical flow estimation. To recover the missing pixels caused by warping, we need to project the corresponding pixels from nearby frames to the target stabilized frame. For each key frame I_k at time $t = k$, we compute the optical flows $\{F_{n \rightarrow k}\}_{n \in \Omega_k}$ from neighboring frames to the key frame using RAFT [Teed and Deng 2020], where n indicates a neighboring frame and Ω_k denotes the set of neighboring frames for the key frame I_k .

Blurry frames removal. For videos with rapid camera or object motion, the input frames may suffer from severe blur. Fusing information from these blurry frames inevitably leads to blurry output. We thus use the method of [Pech-Pacheco et al. 2000] to compute a sharpness score for each neighboring frame and then select the top 50% sharp neighboring frames for fusion. This pre-processing step helps restore sharper contents (see Fig. 4) and improves the runtime.

3.2 Warping and fusion

Warping. We warp the neighboring frames $\{I_n\}_{n \in \Omega_k}$ to align with the target frame $I_{\hat{k}}$ in the virtual camera space. Since we already have the warping field from the target frame to the keyframe $F_{\hat{k} \rightarrow k}$ (estimated from [Yu and Ramamoorthi 2020]) and the estimated optical flow from the keyframe to neighboring frames $\{F_{k \rightarrow n}\}_{n \in \Omega_k}$, we can then compute the warping field from the target frame to neighboring frames $\{F_{\hat{k} \rightarrow n}\}_{n \in \Omega_k}$ by *chaining* the flow vectors. We can thus warp a neighboring frame I_n to align with the target frame $I_{\hat{k}}$ using backward warping. Some pixels in the target frame are not visible in the neighboring frames due to occlusion/dis-occlusion or out-of-boundary. Therefore, we compute visibility mask $\{\alpha_n\}_{n \in \Omega_k}$ for each neighboring frame to indicate whether a pixel is valid (labeled as 1) in the source frame or not. We use the method [Sundaram et al. 2010] to identify occluded pixels (labeled as 0).

Fusion space. With the aligned frames, we explore several fusion strategies. First, we can directly blend the warped color frames in

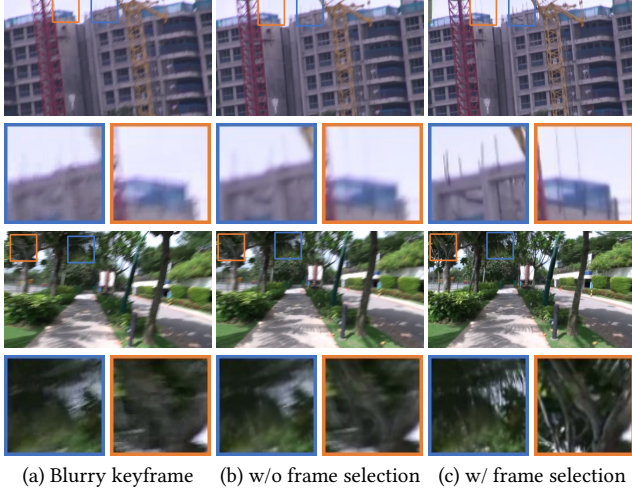


Fig. 4. **Effect of selecting and removing blurred frames.** Rapid camera or object motion leads to blurry frames (a). Stabilizing the videos using all these frames inevitably results in blurry outputs (b). By selecting and removing blurred frames in a video, our method re-renders the stabilized video using only *sharp* input frames and thus can avoid synthesizing blurry frames.

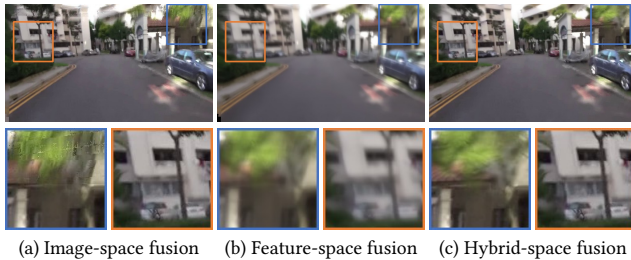


Fig. 5. **Effect of different blending spaces.** (a) Blending multiple frames at the pixel-level retains sharp contents but often leads to visible artifacts due to the sensitivity to flow inaccuracy. (b) Blending in the feature level alleviates these artifacts but has difficulty in generating sharp results. (c) The proposed hybrid-space fusion method is robust to flow inaccuracy and produces sharp output frames.

the *image space* to produce the output stabilized frame, as shown in Fig. 3(a). This image-space fusion approach is a commonly used technique in image stitching [Agarwala et al. 2004; Szeliski 2006], video extrapolation [Lee et al. 2019], and novel view synthesis [Hedman et al. 2018]. However, image-space fusion is prone to generating ghosting artifacts due to misalignment, or glitch artifacts due to inconsistent labeling between neighbor pixels (Fig. 5(a)). Alternatively, one can also fuse the aligned frames in the *feature space* (e.g., [Choi et al. 2019]) (Fig. 3(b)). Fusing in the high-dimensional feature spaces allows the model to be more robust to flow inaccuracy. However, rendering the fused feature map using a neural image-translation decoder often leads to blurry outputs (Fig. 5(b)).

To combine the best worlds of both image-space and feature-space fusions, we propose a *hybrid-space* fusion mechanism for video stabilization (Fig. 3(c)). Similar to the feature-space fusion, we first extract high-dimensional features from each neighboring

frame and warp the features using flow fields. We then learn a CNN to predict the blending weights that best fuse the features. We concatenate the *fused feature map* and the *warped feature for each neighboring frame* to form the input for our image decoder. The image decoder learns to predict a target frame and a confidence map for each neighboring frame. Finally, we adopt an image-space fusion to merge all the predicted target frames according to the predicted weights to generate the final stabilized frame.

The core difference between our hybrid-space fusion and feature-space fusion lies in the input to the image decoder. The image decoder in Fig. 5(b) takes *only* the fused feature as input to predict the output frame. The fused feature map already contains mixed information from multiple frames. The image decoder may thus have difficulty in synthesizing sharp image contents. In contrast, our image decoder in Fig. 5(c) takes the fused feature map as guidance to reconstruct the target frame from the warped feature. We empirically find that this improves the sharpness of the output frame while avoiding ghosting and glitching artifacts, as shown in Fig. 5(c).

Fusion function. In addition to explore *where* should the contents from multiple frames be fused (image, feature, or hybrid), here we discuss *how*. To enable end-to-end training, we consider the following differentiable function for fusion:

1) *Mean fusion*: The simplest approach for fusion is computing the mean of available contents at each location:

$$f_{\text{mean}}^{\hat{k}} = \frac{\sum_{n \in \Omega_k} f_n^{\hat{k}} M_n^{\hat{k}}}{\sum_{n \in \Omega_k} M_n^{\hat{k}} + \tau}, \quad (1)$$

where $f_n^{\hat{k}}$ and $M_n^{\hat{k}}$ is the encoded feature map and warping mask of frame n , respectively. The superscript \hat{k} denotes the encoded feature and warping mask are warped to the stable frame, and τ is a small constant to avoid dividing by zero.

2) *Gaussian-weighted fusion*: Extending the mean fusion by putting larger weights for frames that are temporally closer to the keyframe:

$$f_{\text{gauss}}^{\hat{k}} = \frac{\sum_{n \in \Omega_k} f_n^{\hat{k}} M_n^{\hat{k}} W_n}{\sum_{n \in \Omega_k} M_n^{\hat{k}} W_n + \tau}, \quad (2)$$

where $W_n = G(k, \|n - k\|)$ is the Gaussian blending weight.

3) *Argmax fusion*: Instead of blending (which may cause blur), we can also take the available content that is temporally closest to the keyframe (using the warping mask $M_n^{\hat{k}}$ and the weights W_n).

$$f_{\text{argmax}}^{\hat{k}} = f_{\arg \max_n M_n^{\hat{k}} W_n}. \quad (3)$$

4) *Flow error-weighted fusion*: Instead of the above simple heuristic, we can define the blending weights using the confidence of flow estimate:

$$f_{\text{FE}}^{\hat{k}} = \frac{\sum_{n \in \Omega_k} f_n M_n^{\hat{k}} W_n^{\text{FE}}}{\sum_{n \in \Omega_k} M_n^{\hat{k}} W_n^{\text{FE}} + \tau}, \quad (4)$$

where weights W_n^{FE} is computed by: $W_n^{\text{FE}} = \exp\left(\frac{-e_n^{\hat{k}}}{\beta}\right)$. Here, we use forward-backward flow consistency error $e_n^{\hat{k}}$ to measure the

confidence:

$$e_n(p) = \|\|F_{k \rightarrow n}(p) + F_{n \rightarrow k}(p + F_{k \rightarrow n})\|_2, \quad (5)$$

where p denotes pixel coordinate in $F_{k \rightarrow n}$ and we set $\beta = 0.1$ in all our experiments. In addition, we need to warp the flow error e_n to the target stable frame. We denote the warped flow error as e_n^k .

5) *CNN-based fusion function*: We further explore a *learning-based* fusion function. Specifically, we train a CNN to predict a blending weight for each neighboring frame using the encoded features, visibility masks, and the flow error (Fig. 6).

$$f_n^k = \sum_{n \in \Omega_k} f_n^k \theta(f_n^k, M_n^k, f_k^k, M_k^k, e_n^k), \quad (6)$$

where θ is a CNN followed by soft-max.

After fusing the feature, we concatenate the fused feature with the warped feature and warping mask of each frame as the input to the image decoder. The image decoder then predicts the output color frame and confidence map for each frame:

$$\{I_n^k, C_n^k\} = \phi(f_n^k, M_n^k, f_k^k), \quad (7)$$

where ϕ denotes the image decoder, I_n^k and C_n^k represent the predicted frame and confidence map of frame n in the virtual camera space at time k , respectively. Finally, the output stabilized frame I_k^k is generated by a weighted sum using these predicted frames and confidence maps:

$$I_k^k = \sum_{n \in \Omega_k} I_n^k C_n^k. \quad (8)$$

3.3 Implementation details

Encoding source frames. Before warping and fusion, we encode each source frame $\{I_n\}_{n \in \Omega_k}$ to a higher dimensional feature map. The image encoder consists of 8 ResNet blocks [He et al. 2016] with a stride of 1. All convolutional layers are followed by a ReLU [Nair and Hinton 2010] activation function. The final encoded features are 32-dimensional for each location.

Residual detail transfer. We observe that the output color frames synthesized by the image decoder often does not retain the full high-frequency details as in the input video. We tackle this problem by adopting the residual detail transfer technique similar to [Lu et al. 2020] to add the missing residual details back to output frames, as shown in Fig. 7. Specifically, we feed the warped image feature f_k into the decoder to reconstruct an image and then compute the residual ΔI_k by subtracting the reconstructed image with the input image I_k . Next, we warp the residual using flow $F_{k \rightarrow k}$ to obtain the *warped residual* ΔI_k^k . Finally, we add the warped residual to the decoded image I_k^k before the final fusion stage. This residual detail transfer helps us recover more high-frequency details and improve the overall sharpness of the synthesized frame (see Fig. 8). The use of residual transfer differs from [Lu et al. 2020] in that 1) we transfer the residual to a virtual stabilized frame (as opposed to the original frame) and 2) our method does not require per-scene/video training.

Training. Training our network typically involves unstable-stable video pairs. However, such training data is hard to acquire. We

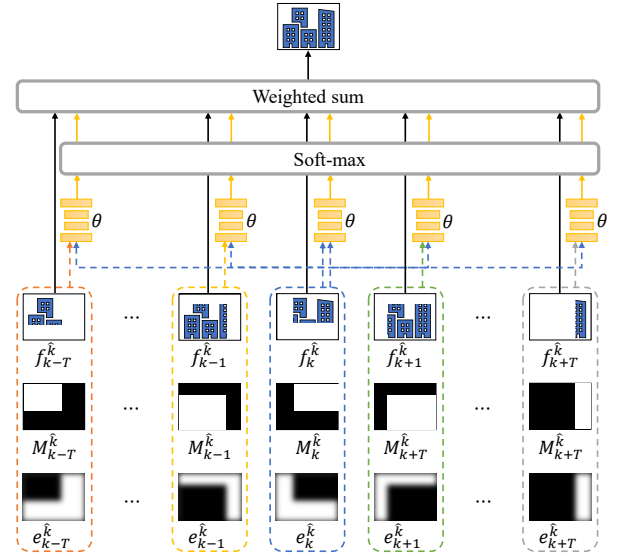


Fig. 6. **Learning-based fusion.** Given the warped features $\{f_n\}_{n \in \Omega_k}$ (or warped images for image-space fusion), warping masks $\{M_n\}_{n \in \Omega_k}$, and the flow error maps $\{e_n\}_{n \in \Omega_k}$, we first concatenate feature, warping mask, and flow error maps for each frame (shown as dotted blocks). We then use a CNN to predict the blending weights for each neighbor frame. Using the predicted weights, we compute the fused feature by weighted averaging the individual warped features $\{f_n\}_{n \in \Omega_k}$.

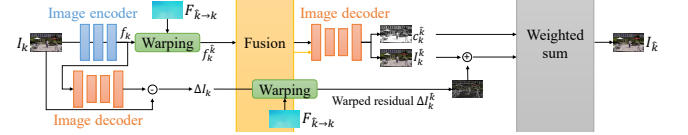


Fig. 7. **Residual detail transfer.** As rendering (warped) image features using a decoder may suffer from loss of high-frequency details, we compute the residuals and transfer them to the target frames to recover these missing details.

thus adopt the leave-one-out protocol [Riegler and Koltun 2020a] to train our network. Specifically, we first sample a short sequence of 7 frames from the training set of [Su et al. 2017] and randomly crop the frames to generate the input *unstable* video. We then apply another random cropping on the center frame as the ground-truth of the keyframe.

Our loss functions include the L1 and VGG perceptual losses:

$$\mathcal{L} = \|\|I_k - I_k^k\|_1 + \sum_l \lambda_l \|\|\psi_l(I_k) - \psi_l(I_k^k)\|_1, \quad (9)$$

where ψ_l are intermediate features from a pre-trained VGG-19 network [Simonyan and Zisserman 2015] and We train our network using the Adam optimizer with a learning learning rate of 0.0001 and default parameters. Our training patch size is 256×256 . We train the model for 50 epochs with a batch size of 1. The training process takes 4 days on a single V100 GPU.

4 EXPERIMENTAL RESULTS

We start with validating various design choices of our approaches (Section 4.1). Next, we present quantitative comparison against representative state-of-the-art video stabilization algorithms (Section 4.2) and visual results (Section 4.3). We conclude the section with a user study (Section 4.4), a runtime analysis (Section 4.5), and discuss limitations (Section 4.6). Furthermore, we present additional detailed experimental results and stabilized videos by the evaluated methods in the supplementary material. We will make the source code and pre-trained model publicly available.

4.1 Ablation study

We analyze the contribution of each design choice, including the fusion function design, fusion mechanism, and residual detail transfer. We use the test set of [Su et al. 2017] for performance evaluation. The test set contains 10 videos (each has 100 frames). We sample sequences of 7 frames in a sliding window fashion and use the center frame as our keyframe. In total, we have $(100 - 3 - 3) \times 10 = 960$ short test sequences (the "3" comes from the beginning/end of the sequences). We generate each testing sequence by randomly cropping 256×256 patches to simulate *unstable* frames (same as the training data generation). We generate another random crop at the center frame in each testing sequence as our target *stabilized* frame. Here we use RAFT [Teed and Deng 2020] to compute the warp field between the two sampled patches at the center frame to simulate the warp field used for stabilizing the video frames.

Fusion function. We train the proposed model using the image-space fusion, feature-space fusion, and hybrid-space fusion with different fusion functions discussed in Fig. 5 and Section 3.2. For image-space fusion, we also include two conventional fusion methods: multi-band blending [Brown et al. 2003] and graph-cut [Agarwala et al. 2004]. We report the quantitative results in Table 1.

For image-space fusion, none of the fusion methods dominate the results, where the argmax and CNN-based fusions perform slightly better than other alternatives. For both feature-space and hybrid-space fusion, the proposed CNN-based fusion shows advantages over other approaches.

Fusion space. Next, we compare different fusion levels (using CNN-based fusion). Table 2 shows that the proposed hybrid-space fusion achieves the best results compared to image-space fusion and feature-space fusion. Fig. 5 shows an example to demonstrate the rendered frames using different fusion spaces. The synthesized frame from the image-space fusion looks sharp but contains visible glitching artifacts due to the discontinuity of different frames and inaccurate motion estimation. The results of the feature-space fusion are smooth but overly blurred. Finally, our hybrid-space fusion takes advantage of both above methods, generating a sharp and artifact-free frame.

Residual detail transfer. Table 3 shows that our residual detail transfer approach helps restore the high-frequency details lost during neural rendering. Fig. 8 shows an example of visual improvement from residual detail transfer.



Fig. 8. **Effect of the residual detail transfer.** The residual detail transfer restores more high-frequency details in the output frames.

4.2 Quantitative evaluation

We evaluate the proposed method with state-of-the-art video stabilization algorithms, including [Grundmann et al. 2011], [Liu et al. 2013], [Wang et al. 2018], [Choi and Kweon 2020], and [Yu and Ramamoorthi 2020], and the warp stabilizer in Adobe Premiere Pro CC 2020. We obtain the results of the compared methods from the videos released by the authors or generated from the publicly available official implementation with default parameters or pre-trained models.

Datasets. We evaluate the above methods on the NUS dataset [Liu et al. 2013] and selfie dataset [Yu and Ramamoorthi 2018]. The NUS dataset consists 144 video sequences, which are classified into six categories: 1) Simple, 2) Quick rotation, 3) Zooming, 4) Parallax, 5) Crowd, and 6) Running. The selfie dataset includes 33 video clips with frontal faces and severe jittering.

Metrics. We use three widely-used metrics to evaluate the performance of video stabilization [Choi et al. 2019; Liu et al. 2013; Wang et al. 2018]: cropping ratio, distortion, and stability. We also include the accumulated optical flow used in Yu et al. [2019] for evaluation. We describe the definition of each evaluation metric in the supplementary material.

Results on the NUS dataset. We show the average scores on the NUS dataset [Liu et al. 2013] on the left side of Table 4 and plot the cumulative score of each metric in the first row of Fig. 9. Both [Choi and Kweon 2020] and our method are full-frame methods and thus have an average cropping ratio of 1. Note that the distortion metric measures the global distortion by fitting a homography between the input and stabilized frames, which is not suitable to measure local distortion. Although [Choi and Kweon 2020] obtain the highest distortion score, their results contain visible local or color distortion due to iterative frame interpolation, as shown in Fig. 10 and our supplementary material. Adobe Premiere Pro 2020 warp stabilizer obtains the highest stability score at the cost of a low cropping ratio (0.74). Our results achieve the lowest accumulated optical flow, the second-best distortion and stability scores, and with an average cropping ratio of 1 (no cropping for all the videos), demonstrating our advantages over the state-of-the-art approaches in the NUS dataset.

Table 1. Quantitative evaluation of fusion functions on the test set of [Su et al. 2017]. We highlight **the best** and **the second best** in each column.

	(a) Image-space fusion			(b) Feature-space			(c) Hybrid-space		
	LPIPS ↓	SSIM ↑	PSNR ↑	LPIPS ↓	SSIM ↑	PSNR ↑	LPIPS ↓	SSIM ↑	PSNR ↑
Multi-band blending	0.105	0.926	26.150	-	-	-	-	-	-
Graph-cut	0.105	0.928	26.190	-	-	-	-	-	-
Mean	0.123	0.899	24.618	0.108	0.878	26.028	0.099	0.898	27.013
Gaussian	0.099	0.920	25.310	0.095	0.874	26.344	0.097	0.899	27.080
Argmax	0.105	0.928	26.200	0.093	0.892	26.891	0.087	0.906	27.519
Flow error-weighted	0.114	0.901	25.363	0.096	0.885	26.176	0.095	0.911	27.371
CNN-based (Ours)	0.101	0.895	26.692	0.092	0.902	27.187	0.073	0.914	27.868

Table 2. Quantitative comparisons on fusion spaces. We use our CNN-based fusion function to compare the performance of three different fusion spaces. See Fig. 5 for visual comparisons.

	LPIPS ↓	SSIM ↑	PSNR ↑
Image-space fusion	0.101	0.895	26.692
Feature-space fusion	0.092	0.902	27.187
Hybrid-space fusion (Ours)	0.073	0.914	27.868

Table 3. Ablation study of residual detail transfer. See Fig. 8 for visual comparisons.

	LPIPS ↓	SSIM ↑	PSNR ↑
w/o residual detail transfer	0.073	0.914	27.868
w/ residual detail transfer	0.056	0.942	29.255

Results on Selfie dataset. We show the average scores on the selfie dataset [Yu and Ramamoorthi 2018] on the right side of Table 4 and plot the cumulative score of each metric in the second row of Fig. 9. Similar to the NUS dataset, our method achieves the best cropping ratio and accumulated optical flow. Our distortion and stability scores are comparable to [Yu and Ramamoorthi 2018], which is specially designed to stabilize selfie videos.

4.3 Visual comparison

We show one stabilized frame of our method and state-of-the-art approaches from the Selfie dataset in Fig. 10. Most of the methods [Grundmann et al. 2011; Liu et al. 2013; Wang et al. 2018; Yu and Ramamoorthi 2020] suffer from a large amount of cropping, as indicated by the green checkerboard regions. The aspect ratios of the output frames are also changed. To keep the same aspect ratio as the input video, more excessive cropping is required. The DIFRINT method [Choi and Kweon 2020] generates full-frame results. However, their results often contain clearly visible artifacts due to frame interpolation. In contrast, our method generates full-frame stabilized videos with fewer visual artifacts. Please refer to our supplementary material for more video comparisons.

4.4 User study

As the quality of video stabilization is a subjective matter of taste, we also conduct a user study to compare the proposed method and three

approaches: [Yu and Ramamoorthi 2020], DIFRINT [Choi and Kweon 2020], and Adobe Premiere Pro 2020 warp stabilizer. We randomly select two videos from the Selfie dataset [Yu and Ramamoorthi 2018] and two videos from each category of the NUS dataset [Liu et al. 2013], resulting in total $2 \times (6 + 1) = 14$ videos for comparison. We adopt the pairwise comparison [Lai et al. 2016; Rubinstein et al. 2010], where each video pair has three questions:

- (1) Which video preserves the most content?
- (2) Which video contains fewer artifacts or distortions?
- (3) Which video is more stable?

The order of the videos is randomly shuffled. The input video is also shown to users as a reference.

From this user study, we collect the results from 46 subjects. We show the winning rate of our method against the compared approaches in Fig. 11. Overall, our results are preferred by the users in more than 60% of the comparisons, demonstrating that the proposed method also outperforms existing approaches in the subjective evaluation.

4.5 Runtime analysis

We measure the runtime of CPU-based approaches [Grundmann et al. 2011; Liu et al. 2013; Yu and Ramamoorthi 2018], on a laptop with i7-8550U CPU. For our method and GPU-based approaches [Choi and Kweon 2020; Wang et al. 2018; Yu and Ramamoorthi 2020], we evaluate on a server with Nvidia Tesla V100 GPU. We use sequence #10 from the Selfie dataset for evaluation, which has a frame resolution of 854×480 . We show the runtime comparisons in Table 5. We also provide the runtime profiling of our method in Table 6. The pre-processing step of motion smoothing from [Yu and Ramamoorthi 2020] takes about 71% of our runtime. Our method can be accelerated by using a more efficient motion smoothing algorithm. However, the quality of warping and fusion also depends on the accuracy of the motion estimation and smoothing.

4.6 Limitations

Video stabilization for videos in unconstrained scenarios remains challenging. Here we discuss several limitations of our approach. We refer to the readers to our supplementary material for video results.

Wobble. When the camera or object motion is too rapid, we observe that the stabilized frame exhibit *rolling shutter wobble* (Fig. 12(a)). Integrating rolling shutter rectification into our approach can potentially alleviate such an issue.

Table 4. Quantitative evaluations with the state-of-the-art methods on the NUS dataset [Liu et al. 2013] and the selfie dataset [Yu and Ramamoorthi 2018]. Red text indicates the best and blue text indicates the second-best performing method.

	NUS dataset [Liu et al. 2013]				Selfie dataset [Yu and Ramamoorthi 2018]			
	Cropping ratio ↑	Distortion value ↑	Stability score ↑	Accumulated optical flow ↓	Cropping ratio ↑	Distortion value ↑	Stability score ↑	Accumulated optical flow ↓
Bundle [Liu et al. 2013]	0.84	0.93	<u>0.84</u>	<u>0.78</u>	0.68	0.76	0.82	0.84
L1Stabilizer [Grundmann et al. 2011]	0.74	0.92	0.82	0.88	0.75	0.92	0.84	0.84
StabNet [Wang et al. 2018]	0.68	0.82	0.81	1.02	0.69	0.79	0.86	0.83
DIFRINT [Choi and Kweon 2020]	1.00	0.97	0.82	0.87	1.00	0.85	0.81	<u>0.72</u>
[Yu and Ramamoorthi 2020]	<u>0.86</u>	0.91	0.83	0.88	0.77	0.83	0.82	0.77
[Yu and Ramamoorthi 2018]	-	-	-	-	<u>0.85</u>	<u>0.89</u>	0.84	0.76
Adobe Premiere Pro 2020 warp stabilizer	0.74	0.83	0.86	0.84	0.70	0.80	<u>0.85</u>	0.79
Ours	1.00	<u>0.96</u>	<u>0.84</u>	0.77	1.00	0.86	0.84	0.64

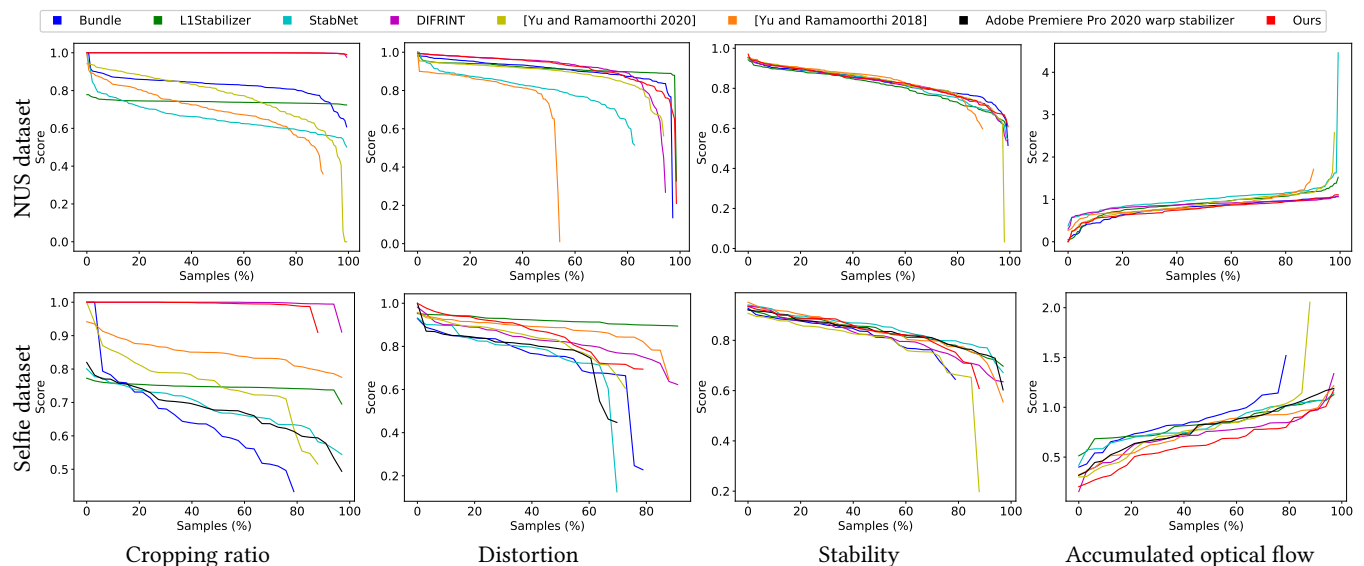


Fig. 9. Quantitative evaluation on the NUS dataset [Liu et al. 2013] and the selfie dataset [Yu and Ramamoorthi 2018]. As some of the methods fail to produce results for several sequences, computing averaged scores of successful sequences does not reflect the robustness of the method. For each method, we store all the error metrics for each sequence and plot the *sorted* scores. These plots reflect both the *completeness* and the *performance* (in cropping ratio, distortion, stability, and smoothness). Our approach achieves full-frame stabilization (except for a few sequences where [Yu and Ramamoorthi 2020] fails to generate results) while maintaining competitive performance compared with the state-of-the-art.

Table 5. Per-frame runtime comparison. CPU-based methods are evaluated on a laptop with i7-8550U CPU, while GPU-based methods are evaluated on a server with Nvidia Tesla V100 GPU. The testing video has a frame resolution of 854×480. *: Time is reported in [Yu and Ramamoorthi 2018] as the source code is not available.

Method	Environment	Implementation	Runtime (s)
L1Stabilizer [Grundmann et al. 2011]	CPU	Matlab	0.623
Bundle [Liu et al. 2013]	CPU	Matlab	7.612
StabNet [Wang et al. 2018]	GPU	TensorFlow	0.073
DIFRINT [Choi and Kweon 2020]	GPU	PyTorch	1.627
[Yu and Ramamoorthi 2020]	GPU	PyTorch	6.501
[Yu and Ramamoorthi 2018]	CPU	Matlab	15 mins*
Adobe Premiere Pro 2020 warp stabilizer	CPU	-	0.045
Ours excluding [Yu and Ramamoorthi 2020]	GPU	PyTorch	3.090
Ours	GPU	PyTorch	9.591

Table 6. Runtime breakdown of the proposed method.

Stage	Runtime (s)	Percentage
Motion smoothing [Yu and Ramamoorthi 2020]	6.826	71.03%
Image encoder	0.724	7.53%
Warping	0.207	2.15%
CNN-based fusion	0.952	9.91%
Image decoder	0.881	9.17%
Final fusion	0.020	0.21%

Visible seams. As our method fuse multiple frames to re-render a stabilized frame, our results may contain visible seams, particularly when there are large lighting variations caused by camera white-balancing and exposure corrections (Fig. 12(b)).



Fig. 10. **Visual comparison to state-of-the-art methods.** Our proposed fusion approach does not suffer from aggressive cropping of frame borders and renders stabilized frames with significantly fewer artifacts than DIFRINT [Choi and Kweon 2020]. We refer the readers to our supplementary material for extensive video comparisons with prior representative methods.

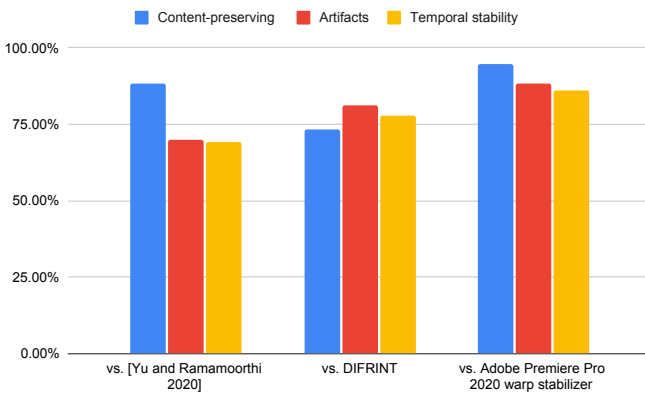


Fig. 11. **User preference of our method against other state-of-the-art methods.** We ask the subjects to rate their preferences over the video stabilization results in a randomized paired comparison (ours vs. other) in terms of content preservation, visual artifacts, and temporal stability. Overall our results are preferred by the users in all aspects.

Temporal flicker and distortion. Our method builds upon an existing motion smoothing method [Yu and Ramamoorthi 2020] to obtain stabilized frames. However, the method [Yu and Ramamoorthi 2020] may produce temporally flickering results due to large non-rigid occlusion and inconstant foreground/background motion (e.g., selfie videos). In such cases, due to the dependency of motion inpainting, our method also suffers from undesired temporal flicker and distortion (Fig. 12(c)).

Speed. Our work aims for offline application. Currently, our method runs slowly (about 10 seconds/frame) compared to many existing methods. Speeding up the runtime is an important future work.

5 CONCLUSIONS

We have presented a novel method for full-frame video stabilization. Our core idea is to develop a learning-based fusion approach to aggregate warped contents from multiple neighboring frames

in a robust manner. We explore several design choices, including early/late fusion, heuristic/learned fusion weights, and residual detail transfer, and provide a systematic ablation study to validate the contributions of each individual component. Experiment results on two public benchmark datasets demonstrate that our method compares favorably against state-of-the-art video stabilization algorithms.

REFERENCES

- Aseem Agarwala, Mira Dontcheva, Maneesh Agrawala, Steven Drucker, Alex Colburn, Brian Curless, David Salesin, and Michael Cohen. 2004. Interactive digital photomontage. In *ACM TOG*.
- Kara-Ali Aliev, Dmitry Ulyanov, and Victor Lempitsky. 2020. Neural point-based graphics. (2020).
- Matthew Brown, David G Lowe, et al. 2003. Recognising panoramas.. In *ICCV*.
- Chris Buehler, Michael Bosse, and Leonard McMillan. 2001a. Non-metric image-based rendering for video stabilization. In *CVPR*.
- Chris Buehler, Michael Bosse, Leonard McMillan, Steven Gortler, and Michael Cohen. 2001b. Unstructured lumigraph rendering. In *Proceedings of the 28th Annual Conference on Computer Graphics and Interactive Techniques*.
- Gaurav Chaurasia, Sylvain Duchene, Olga Sorkine-Hornung, and George Drettakis. 2013. Depth synthesis and local warps for plausible image-based navigation. *ACM Transactions on Graphics (TOG)* 32, 3 (2013), 1–12.
- Shenchang Eric Chen and Lance Williams. 1993. View interpolation for image synthesis. In *Proceedings of the 20th Annual Conference on Computer Graphics and Interactive Techniques*. 279–288.
- Inchang Choi, Orazio Gallo, Alejandro Troccoli, Min H Kim, and Jan Kautz. 2019. Extreme view synthesis. In *ICCV*.
- Jinsoo Choi and In So Kweon. 2020. Deep iterative frame interpolation for full-frame video stabilization. *ACM TOG* (2020).
- Paul E Debevec, Camillo J Taylor, and Jitendra Malik. 1996. Modeling and rendering architecture from photographs: A hybrid geometry-and image-based approach. In *Proceedings of the 23rd Annual Conference on Computer Graphics and Interactive Techniques*. 11–20.
- Chen Gao, Ayush Saraf, Jia-Bin Huang, and Johannes Kopf. 2020. Flow-edge Guided Video Completion. In *ECCV*.
- Michael L Gleicher and Feng Liu. 2008. Re-cinematography: Improving the camerawork of casual video. *ACM Transactions on Multimedia Computing, Communications, and Applications (TOMM)* (2008).
- Amit Goldstein and Raanan Fattal. 2012. Video stabilization using epipolar geometry. *ACM TOG* (2012).
- Steven J Gortler, Radek Grzeszczuk, Richard Szeliski, and Michael F Cohen. 1996. The lumigraph. In *Proceedings of the 23rd Annual Conference on Computer Graphics and Interactive Techniques*. 43–54.
- Matthias Grundmann, Vivek Kwatra, Daniel Castro, and Irfan Essa. 2012. Calibration-free rolling shutter removal. In *ICCP*.



(a) Wobble

(b) Visible seams

(c) Temporal flicker and distortion

Fig. 12. Limitations. (a) Our method does not correct rolling shutter and thus may suffer wobble artifacts. (b) Our fusion approach is not capable of compensating large photometric variations across frames, resulting in visible seams. (c) Existing smoothing approach [Yu and Ramamoorthi 2020] may introduce distortion, particularly when videos contain non-rigid large occlusion (such as selfie videos). As our method depends on the flow produced by [Yu and Ramamoorthi 2020] for stabilizing the video, we cannot correct such errors.

Matthias Grundmann, Vivek Kwatra, and Irfan Essa. 2011. Auto-directed video stabilization with robust ℓ_1 optimal camera paths. In *CVPR*.

Kaiming He, Xiangyu Zhang, Shaoqing Ren, and Jian Sun. 2016. Deep residual learning for image recognition. In *CVPR*.

Peter Hedman, Julian Philip, True Price, Jan-Michael Frahm, George Drettakis, and Gabriel Brostow. 2018. Deep blending for free-viewpoint image-based rendering. *ACM TOG* (2018).

Jia-Bin Huang, Sing Bing Kang, Narendra Ahuja, and Johannes Kopf. 2016. Temporally coherent completion of dynamic video. *ACM TOG* (2016).

Johannes Kopf, Michael F Cohen, and Richard Szeliski. 2014. First-person hyper-lapse videos. *ACM TOG* (2014).

Johannes Kopf, Kevin Matzen, Suhib Alsian, Ocean Quigley, Francis Ge, Yangming Chong, Josh Patterson, Jan-Michael Frahm, Shu Wu, Matthew Yu, et al. 2020. One shot 3D photography. *ACM Transactions on Graphics (TOG)* 39, 4 (2020), 76–1.

Wei-Sheng Lai, Jia-Bin Huang, Zhe Hu, Narendra Ahuja, and Ming-Hsuan Yang. 2016. A comparative study for single image blind deblurring. In *CVPR*.

Ken-Yi Lee, Yung-Yu Chuang, Bing-Yu Chen, and Ming Ouhyoung. 2009. Video stabilization using robust feature trajectories. In *ICCV*.

Sangwoo Lee, Jungjin Lee, Bumki Kim, Kyehyun Kim, and Junyong Noh. 2019. Video Extrapolation Using Neighboring Frames. *ACM TOG* (2019).

Marc Levoy and Pat Hanrahan. 1996. Light field rendering. In *Proceedings of the 23rd Annual conference on Computer Graphics and Interactive Techniques*. 31–42.

Zhengqi Li, Simon Niklaus, Noah Snavely, and Oliver Wang. 2020. Neural Scene Flow Fields for Space-Time View Synthesis of Dynamic Scenes. *arXiv preprint arXiv:2011.13084* (2020).

Feng Liu, Michael Gleicher, Hailin Jin, and Aseem Agarwala. 2009. Content-preserving warps for 3D video stabilization. *ACM TOG* (2009).

Feng Liu, Michael Gleicher, Jue Wang, Hailin Jin, and Aseem Agarwala. 2011. Subspace video stabilization. *ACM TOG* (2011).

Shuaicheng Liu, Yinting Wang, Lu Yuan, Jiajun Bu, Ping Tan, and Jian Sun. 2012. Video stabilization with a depth camera. In *CVPR*.

Shuaicheng Liu, Lu Yuan, Ping Tan, and Jian Sun. 2013. Bundled camera paths for video stabilization. *ACM TOG* (2013).

Shuaicheng Liu, Lu Yuan, Ping Tan, and Jian Sun. 2014. Steadyflow: Spatially smooth optical flow for video stabilization. In *CVPR*.

Stephen Lombardi, Tomas Simon, Jason Saragih, Gabriel Schwartz, Andreas Lehrmann, and Yaser Sheikh. 2019. Neural volumes: Learning dynamic renderable volumes from images. *ACM TOG* (2019).

Erika Lu, Forrester Cole, Tali Dekel, Weidi Xie, Andrew Zisserman, David Salesin, William T Freeman, and Michael Rubinstein. 2020. Layered neural rendering for retiming people in video. *ACM TOG* (2020).

Yasuyuki Matsushita, Eyal Ofek, Xiaou Tang, and Heung-Yeung Shum. 2005. Full-frame video stabilization. In *CVPR*.

Ben Mildenhall, Pratul P Srinivasan, Matthew Tancik, Jonathan T Barron, Ravi Ramamoorthi, and Ren Ng. 2020. Nerf: Representing scenes as neural radiance fields for view synthesis. In *ECCV*.

Vinod Nair and Geoffrey E Hinton. 2010. Rectified linear units improve restricted boltzmann machines. In *ICML*.

Simon Niklaus, Long Mai, Jimei Yang, and Feng Liu. 2019. 3D Ken Burns effect from a single image. *ACM TOG* (2019).

José Luis Pech-Pacheco, Gabriel Cristóbal, Jesús Chamorro-Martínez, and Joaquín Fernández-Valdivia. 2000. Diatom autofocusing in brightfield microscopy: a comparative study. In *ICPR*.

Eric Penner and Li Zhang. 2017. Soft 3D reconstruction for view synthesis. *ACM Transactions on Graphics (TOG)* 36, 6 (2017), 1–11.

Gernot Riegler and Vladlen Koltun. 2020a. Free view synthesis. In *ECCV*. 623–640.

Gernot Riegler and Vladlen Koltun. 2020b. Stable View Synthesis. *arXiv preprint arXiv:2011.07233* (2020).

Michael Rubinstein, Diego Gutierrez, Olga Sorkine, and Ariel Shamir. 2010. A comparative study of image retargeting. In *ACM SIGGRAPH Asia*.

Steven M Seitz and Charles R Dyer. 1996. View morphing. In *Proceedings of the 23rd Annual Conference on Computer Graphics and Interactive Techniques*.

Meng-Li Shih, Shih-Yang Su, Johannes Kopf, and Jia-Bin Huang. 2020. 3d photography using context-aware layered depth inpainting. In *CVPR*.

Karen Simonyan and Andrew Zisserman. 2015. Very deep convolutional networks for large-scale image recognition. (2015).

Vincent Sitzmann, Justus Thies, Felix Heide, Matthias Nießner, Gordon Wetzstein, and Michael Zollhöfer. 2019a. Deepvoxels: Learning persistent 3d feature embeddings. In *CVPR*.

Vincent Sitzmann, Michael Zollhöfer, and Gordon Wetzstein. 2019b. Scene representation networks: Continuous 3d-structure-aware neural scene representations.

Brandon M Smith, Li Zhang, Hailin Jin, and Aseem Agarwala. 2009. Light field video stabilization. In *ICCV*.

Pratul P Srinivasan, Richard Tucker, Jonathan T Barron, Ravi Ramamoorthi, Ren Ng, and Noah Snavely. 2019. Pushing the boundaries of view extrapolation with multiplane images. In *CVPR*.

Shuochen Su, Mauricio Delbracio, Jue Wang, Guillermo Sapiro, Wolfgang Heidrich, and Oliver Wang. 2017. Deep video deblurring for hand-held cameras. In *CVPR*.

Narayanan Sundaram, Thomas Brox, and Kurt Keutzer. 2010. Dense point trajectories by GPU-accelerated large displacement optical flow. In *ECCV*.

Richard Szeliski. 2006. Image alignment and stitching: A tutorial. *Foundations and Trends® in Computer Graphics and Vision* 2, 1 (2006), 1–104.

Zachary Teed and Jia Deng. 2020. RAFT: Recurrent All-Pairs Field Transforms for Optical Flow. (2020).

Justus Thies, Michael Zollhöfer, and Matthias Nießner. 2019. Deferred neural rendering: Image synthesis using neural textures. *ACM TOG* (2019).

Edgar Tretschk, Ayush Tewari, Vladislav Golyanik, Michael Zollhöfer, Christoph Lassner, and Christian Theobalt. 2020. Non-Rigid Neural Radiance Fields: Reconstruction and Novel View Synthesis of a Deforming Scene from Monocular Video. *arXiv preprint arXiv:2012.12247* (2020).

Miao Wang, Guo-Ye Yang, Jin-Kun Lin, Song-Hai Zhang, Ariel Shamir, Shao-Ping Lu, and Shi-Min Hu. 2018. Deep online video stabilization with multi-grid warping transformation learning. *IEEE Transactions on Image Processing* (2018).

Yu-Shuen Wang, Feng Liu, Pu-Sheng Hsu, and Tong-Yee Lee. 2013. Spatially and temporally optimized video stabilization. *IEEE Transactions on Visualization and Computer Graphics* (2013).

Olivia Wiles, Georgia Gkioxari, Richard Szeliski, and Justin Johnson. 2020. Synsin: End-to-end view synthesis from a single image. In *CVPR*.

Shangzhe Wu, Christian Rupprecht, and Andrea Vedaldi. 2020. Unsupervised learning of probably symmetric deformable 3d objects from images in the wild. In *CVPR*.

Wenqi Xian, Jia-Bin Huang, Johannes Kopf, and Changil Kim. 2020. Space-time Neural Irradiance Fields for Free-Viewpoint Video. *arXiv preprint arXiv:2011.12950* (2020).

Sen-Zhe Xu, Jun Hu, Miao Wang, Tai-Jiang Mu, and Shi-Min Hu. 2018. Deep video stabilization using adversarial networks. In *Computer Graphics Forum*.

Jiayang Yu and Ravi Ramamoorthi. 2018. Selfie video stabilization. In *ECCV*.

Jiayang Yu and Ravi Ramamoorthi. 2019. Robust video stabilization by optimization in cnn weight space. In *CVPR*.

Jiayang Yu and Ravi Ramamoorthi. 2020. Learning Video Stabilization Using Optical Flow. In *CVPR*.

Tinghui Zhou, Richard Tucker, John Flynn, Graham Fyffe, and Noah Snavely. 2018. Stereo magnification: Learning view synthesis using multiplane images. *ACM TOG* (2018).

Zihan Zhou, Hailin Jin, and Yi Ma. 2013. Plane-based content preserving warps for video stabilization. In *CVPR*.